Journal of Geophysical Research: Solid Earth

Supporting Information for

Inflation and Asymmetric Collapse at Kilauea Summit during the 2018 Eruption from Seismic and Infrasound Analyses

Voon Hui Lai[1,2], Zhongwen Zhan[1],
Quentin Brissaud[1,3], Osamu Sandanbata[4] and Meghan S. Miller[2]

[1]Seismological Laboratory, California Institute of Technology, USA.
[2]Research School of Earth Sciences, The Australian National University, Australia
[3]Norwegian Seismic Array (NORSAR), Norway.
[4]National Research Institute for Earth Science and Disaster Resilience, Japan.

Corresponding author: Voon Hui Lai (voonhui.lai@anu.edu.au)

Contents of this file

Additional Supporting Information

Introduction

Supporting information contains the description of moment tensor decomposition for very long period teleseismic inversion (Text S1), the procedure for the teleseismic inversion (Text S2), supplementary figures referenced in the main text (Figures S1 to S16), and captions for the two moment tensor catalogs produced using the local and global data (Dataset S1 and S2).

Text S1. Moment tensor decomposition for very long period teleseismic inversion

In Section 5.2 of Main Text, we decompose moment tensors into three components, vertical-CLVD (vCLVD), vertical dip-slip (DS), and vertical strike-slip (SS) components, following Sandanbata et al. (2021). First, we define three moment scales corresponding to isotropic (*ISO*), vertical-CLVD (*vCLVD*), and difference (*D*) components with the three diagonal elements (M_{rr}, $M_{\theta\theta}$, and $M_{\phi\phi}$):

$$M_{vCLVD} = \frac{1}{3}\left(2M_{rr} - M_{\theta\theta} - M_{\phi\phi}\right), \quad (1)$$

and

$$M_D = \frac{1}{2}\left(M_{\theta\theta} - M_{\phi\phi}\right). \quad (2)$$

Note that ring-faulting has no isotropic component is contained ($M_{ISO} = M_{rr} + M_{\theta\theta} + M_{\phi\phi} = 0$). Using the two moment scales (M_{vCLVD} and M_D) and the non-diagonal elements ($M_{r\theta}$, $M_{r\phi}$, and $M_{\theta\phi}$), the moment tensor is decomposed into three components, vCLVD, SS, and DS, respectively, in the following form:

$$\boldsymbol{M} = \boldsymbol{M}_{vCLVD} + \boldsymbol{M}_{SS} + \boldsymbol{M}_{DS}, \quad (3)$$

where

$$\boldsymbol{M}_{vCLVD} = M_{vCLVD}\begin{bmatrix} -1 & & \\ 0 & 0.5 & \\ 0 & 0 & 0.5 \end{bmatrix}, \quad (4)$$

$$\boldsymbol{M}_{SS} = \boldsymbol{M}_D + \boldsymbol{M}_{\theta\phi} = M_D\begin{bmatrix} 0 & & \\ 0 & 1 & \\ 0 & 0 & -1 \end{bmatrix} + M_{\theta\phi}\begin{bmatrix} 0 & & \\ 0 & 0 & \\ 0 & 1 & 0 \end{bmatrix}, \quad (5)$$

and

$$\boldsymbol{M}_{DS} = \boldsymbol{M}_{r\theta} + \boldsymbol{M}_{r\phi} = M_{r\theta}\begin{bmatrix} 0 & & \\ 1 & 0 & \\ 0 & 0 & 0 \end{bmatrix} + M_{r\phi}\begin{bmatrix} 0 & & \\ 0 & 0 & \\ 1 & 0 & 0 \end{bmatrix}. \quad (6)$$

The sign of M_{CLVD} in Equation (3) depends on the type of vertical-CLVD component: $M_{CLVD} > 0$ for vertical-T CLVD, and $M_{CLVD} < 0$ for vertical-P CLVD. Then the moment scales of the SS and DS components are defined by $M_{SS} = \sqrt{M_D^2 + M_{\theta\phi}^2}$, and $M_{DS} = \sqrt{M_{r\theta}^2 + M_{r\phi}^2}$, respectively.

Using the two components that are resolvable from very long-period seismic waves at far field, i.e., $\boldsymbol{M}_{vCLVD}$ and $\boldsymbol{M}_{SS}$, the resolvable moment tensor is defined as

$$\boldsymbol{M}_{RES} = \boldsymbol{M}_{vCLVD} + \boldsymbol{M}_{SS}. \quad (7)$$

Using the moment scales of the two resolbable components, the CLVD ratio (k_{CLVD}) is defined as

$$k_{CLVD} = \frac{|M_{vCLVD}|}{|M_{vCLVD}| + M_{SS}} \times 100\ [\%], \quad (8)$$

which is a function of the arc angle of the ring fault (Fig. S11c). The P-axis axis of $\boldsymbol{M}_{SS}$ can be used as a proxy of t the orientation of the fault plane measured at the midpoint of the curved fault (Figure S11d).

Text S2. Procedure for very long period teleseismic inversion

In Section 5.2 of Main Text, to estimate source parameters of the ring fault, we performed the moment tensor inversion for the 50 collapse events using very long period teleseismic waveforms with the zero-trace constraint ($M_{ISO} = M_{rr} + M_{\theta\theta} + M_{\phi\phi} = 0$). We use the W-phase code for the inversion process, including the filtering, data screening and computation of the Green's functions (Kanamori and Rivera, 2008; Hayes et al., 2009; Duputel et al., 2012). The Green's functions are normal modes generated from 1D PREM model, with waveforms filtered between 0.005 and 0.01 Hz. The centroid location is simply assumed at the caldera center at 0.5 km depth below the solid surface, as a case study demonstrated that these resolvable components are well-constrained even with uncertainty in centroid location and depth (Sandanbata et al., 2021). We used the vertical component of broad-band seismic records at stations ranging from 15° to 90° in epicentral distance. Using $\boldsymbol{M}_{RES}$ extracted from the obtained moment tensor, we determined k_{CLVD} and the P-axis direction of $\boldsymbol{M}_{SS}$ (Figures S13, and red dots in Figure S14). To consider the bias in the estimation of $\boldsymbol{M}_{RES}$ caused by a positive isotropic source close to the ring fault, we additionally conducted the inversion with the constraint of M_{ISO} = 4.23x10^{16} Nm. We found that the positive isotropic source only reduced our estimate of k_{CLVD} (black dots Figure S14).

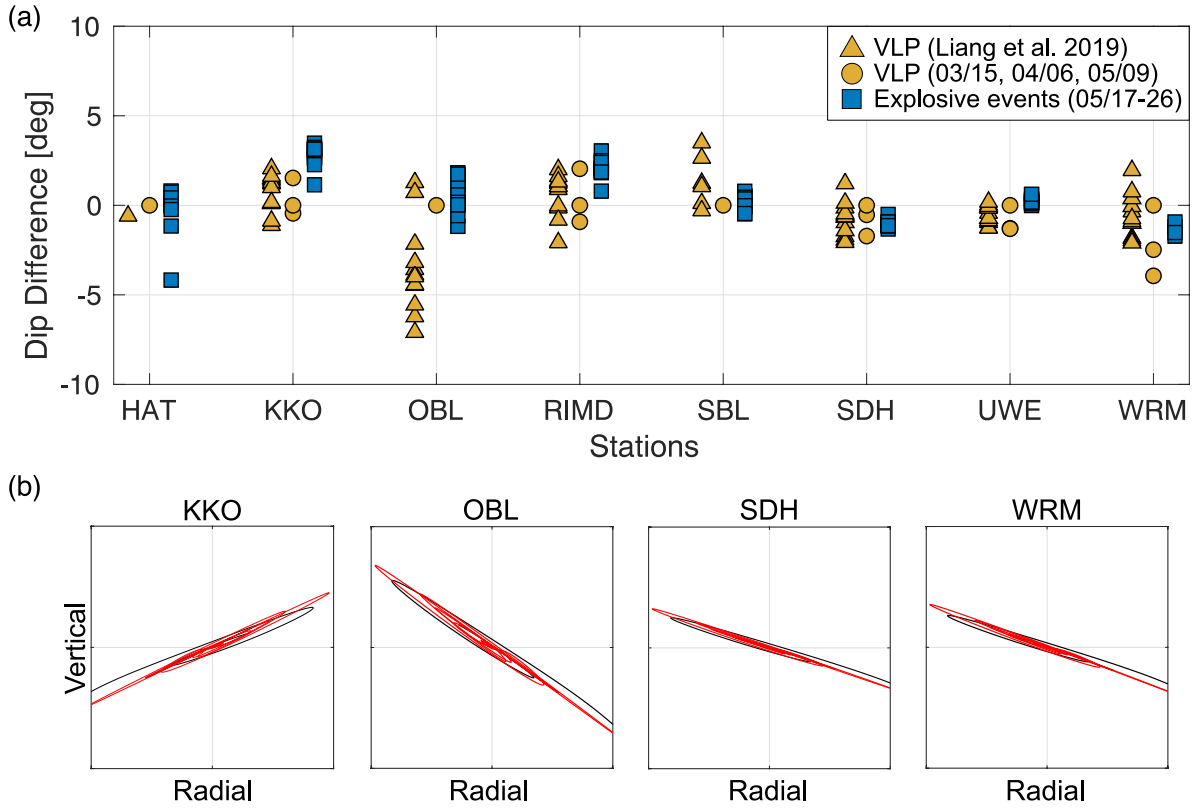

Figure S1:
(a) Graph shows the difference in measured dip of the reference Very Long Period (VLP) event on 05/09 to other VLP events prior to 05/17 (i.e., 03/15, 04/06 and events studied by Liang et al. (2019) between 05/03 and 05/07) and the explosive seismic events (05/17 to 05/26). Dip is measured from the radial and vertical particle motions filtered at 0.02 – 0.05 Hz. The radial component is obtained by rotating the horizontal particle motions according to the observed azimuths in Figure 2. The difference in dip among events is small, indicating a great overlapping of particle motion and that the seismic source for the events is at similar depth. Station OBL shows the greatest variation due to close proximity to the source and steep topography. (b) Plots show the comparison of particle motions from the reference VLP event (black) to explosive event 2 (05/17b; red) at station KKO, OBL, SDH, and WRM.

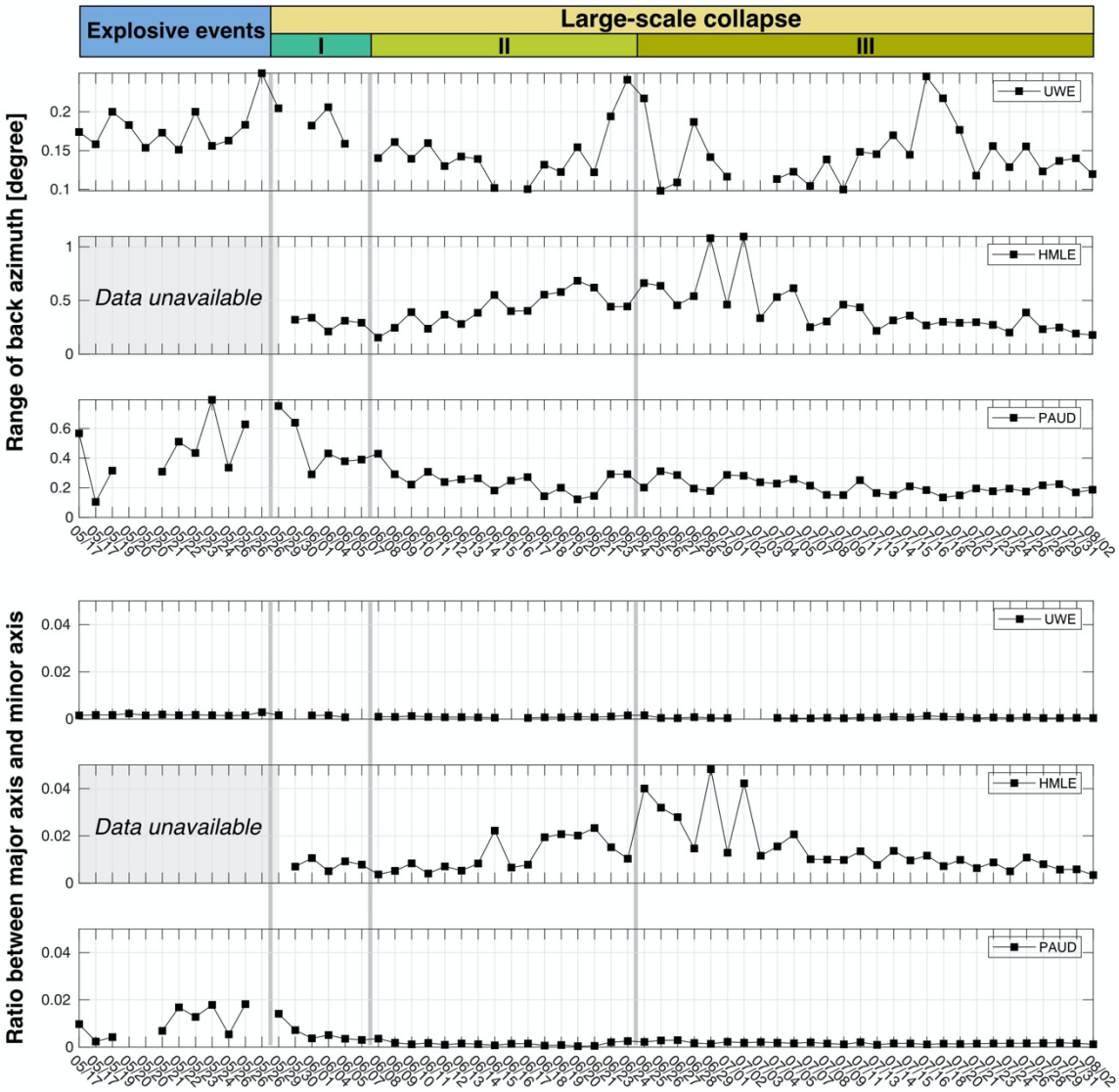

Figure S2:
Top graph shows the range of back azimuths measured using bootstrapping method for each station. Overall, the particle motions have a small range (generally less than 0.5 degree). Bottom graph shows the ratio between the major axis and minor axis of the ellipsoidal particle motion. Small ratio indicates high rectilinearity. Measurements with larger than average ratio also have a large range in the back azimuths measurement.

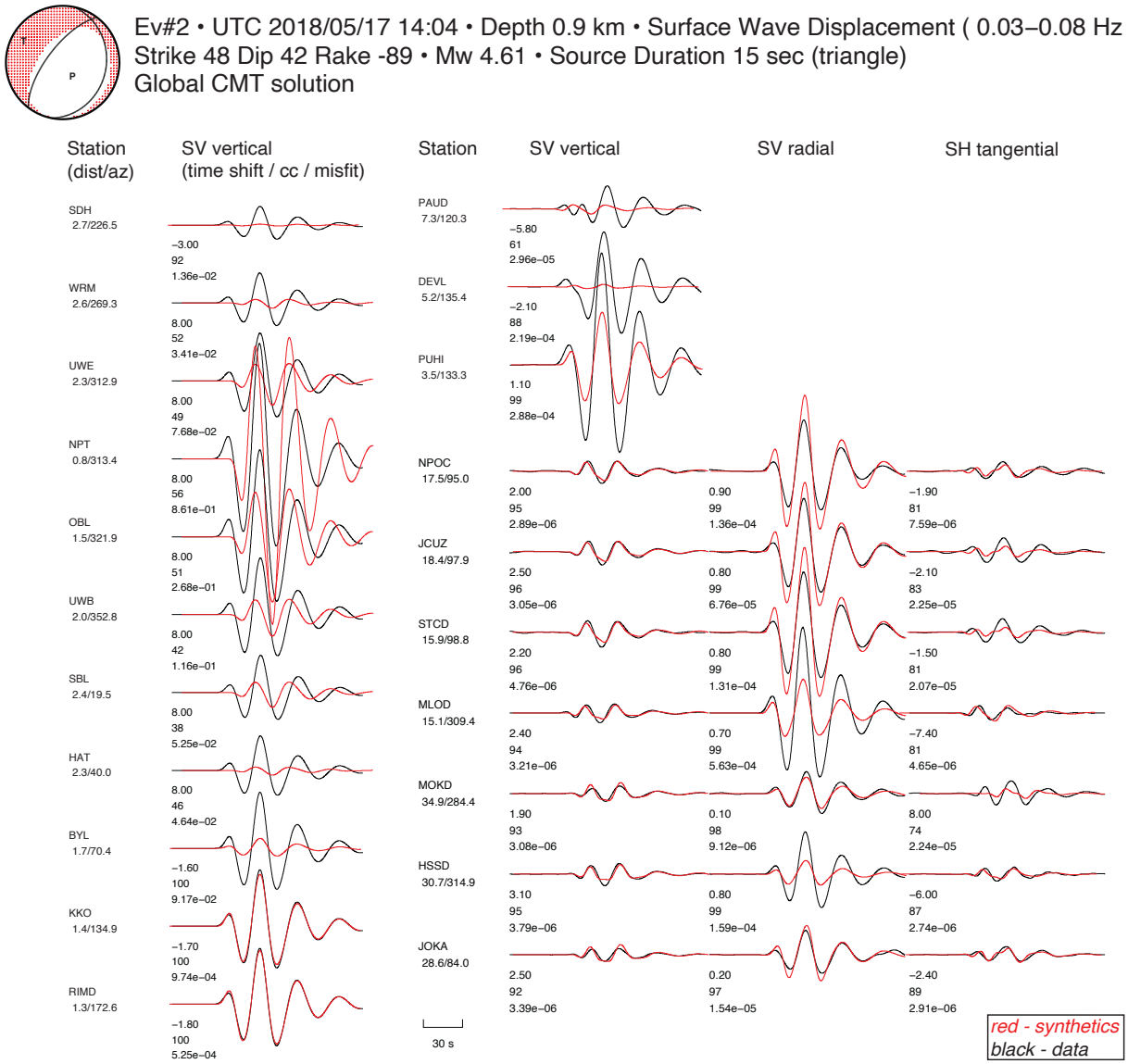

Figure S3:
Figure shows the waveform fitting of synthetics (red) from the global Centroid Moment Tensor (GCMT) solution to the observed data (black) for explosive event 2 (2018/05/17b). The waveforms are surface wave displacement filtered at 0.03 – 0.08 Hz. The waveforms are allowed to shift in time to maximize the correlation coefficient value. The GCMT solution fits the regional waveforms but does not fit the vertical components from stations less than 10 km away from the summit.

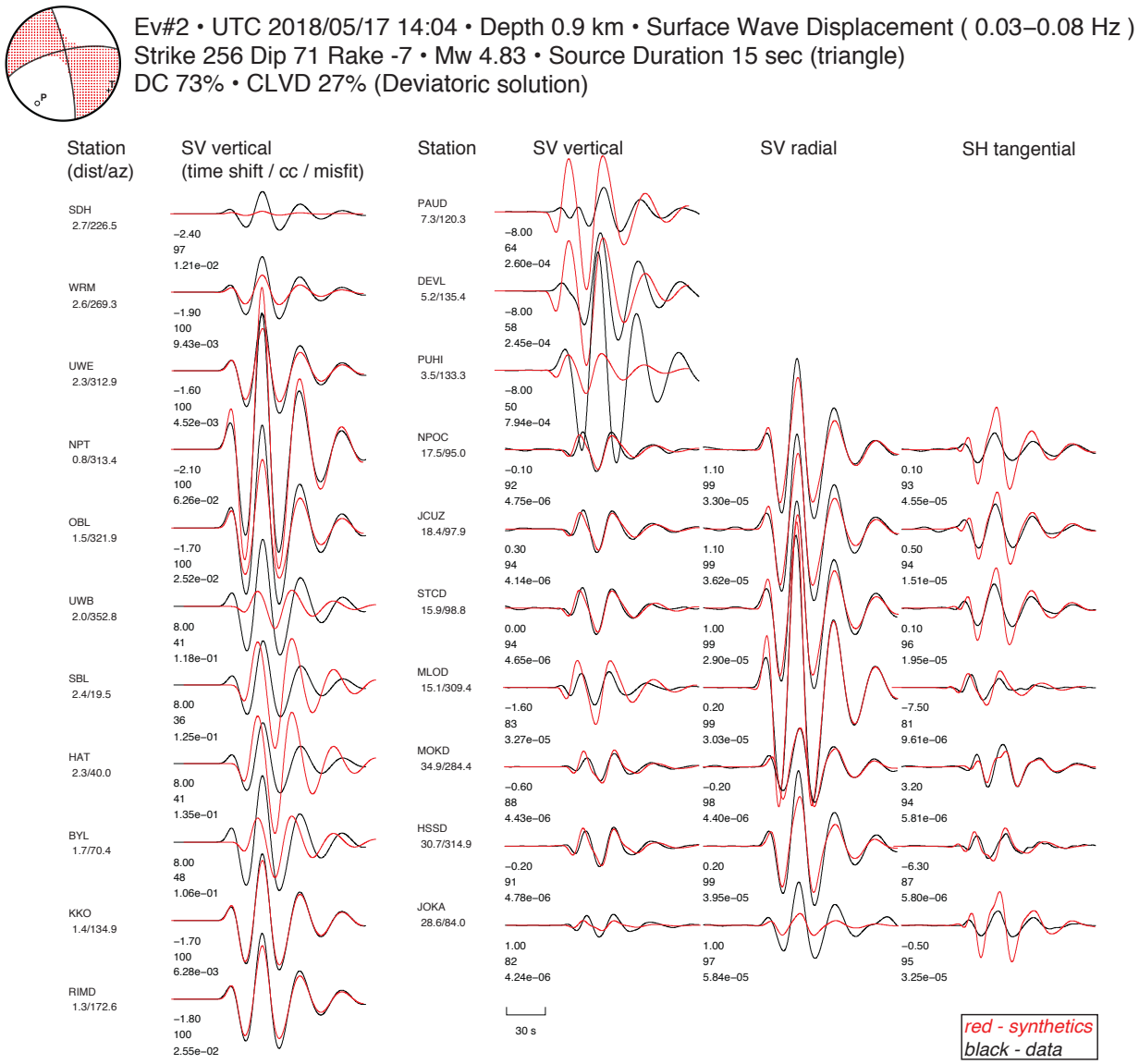

Figure S4:
Figure shows the waveform fitting of synthetics (red) from the best-fitting deviatoric solution inverted using gCAP to the observed data (black) for explosive event 2 (2018/05/17b). The waveforms are surface wave displacement filtered at 0.03 – 0.08 Hz. The deviatoric solution fits the regional waveforms but does not fit all the vertical components from stations less than 10 km away from the summit.

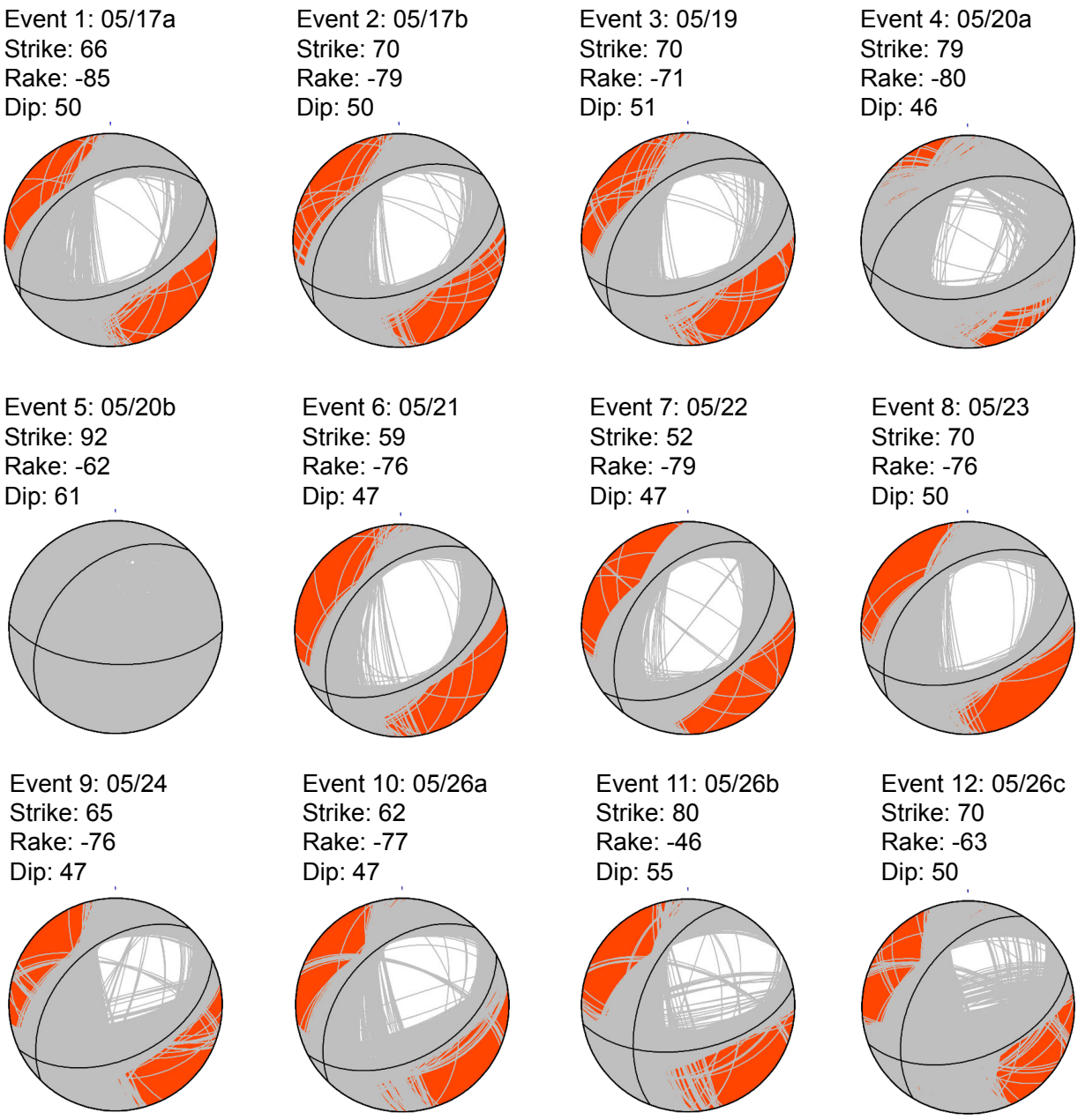

Figure S5:
Figure shows the bootstrapping results of the strike, rake, and dip for explosive events between 05/17 and 05/26. The focal mechanism shows the double-couple contribution, the nodal planes from the bootstrapping (grey), and the preferred nodal planes (black) from the best-fitting full moment tensor solution. All events, except for Event 4 and 5, show consistent strike, rake, and dip.

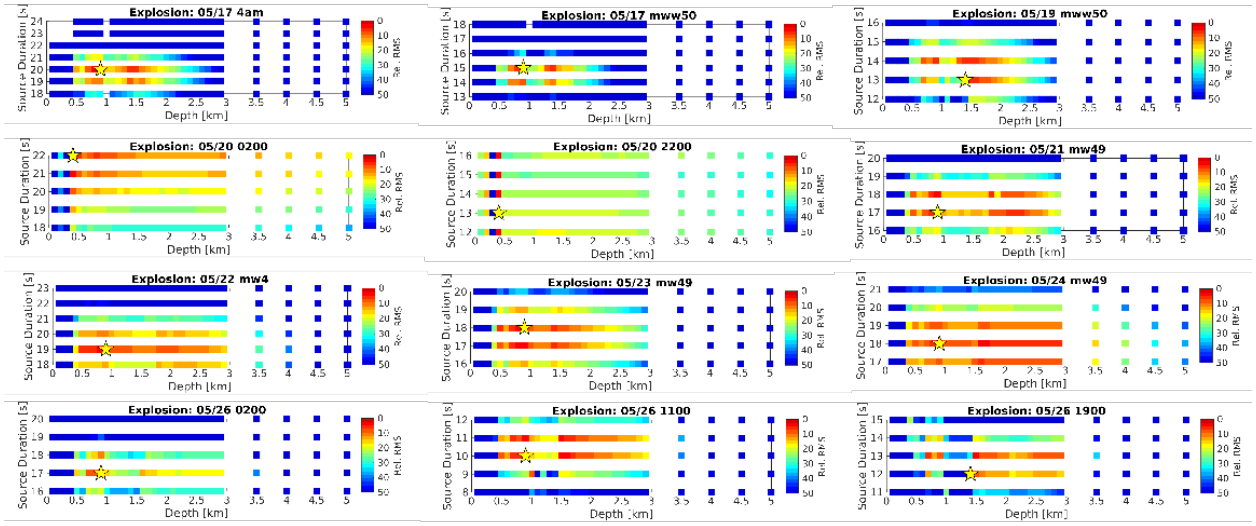

Figure S6:
Figure shows the misfits of the gCAP full moment tensor solutions for a range of source duration and depth for the explosive events between 05/17 and 05/26. The root mean square (RMS) misfit is scaled to the best-fit solution for each event, which is marked by the yellow star. Most events prefer depths between 0.7 and 2.0 km, with the best solution 900 m from the surface. The preferred source duration is independent for each event. Event 4 and 5 (05/20) have complicated waveforms hence resulting in poor grid search results.

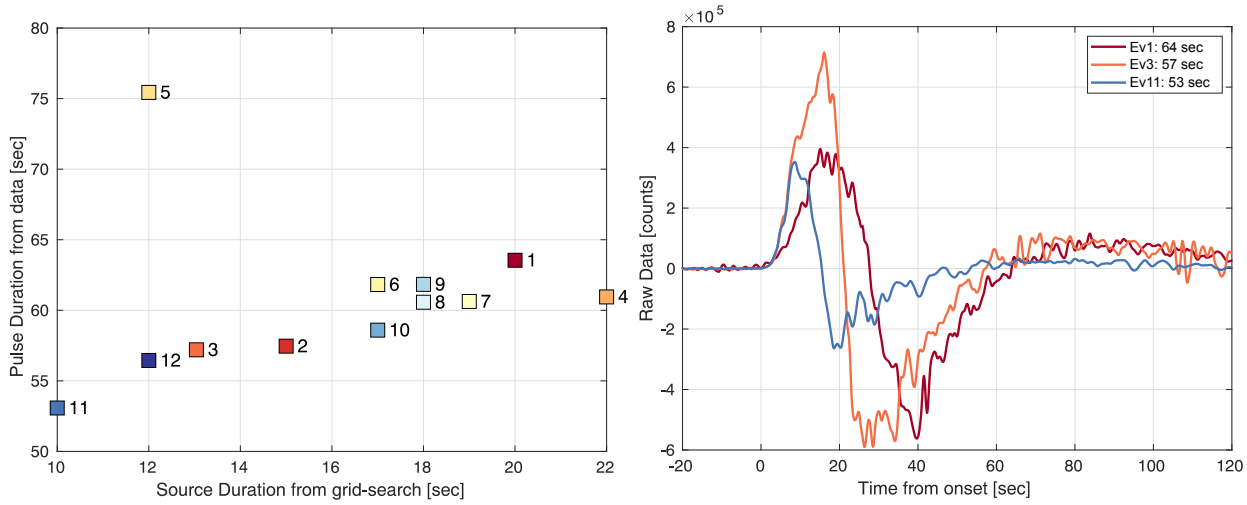

Figure S7:
Left graph shows a strong correlation between the measured pulse duration from raw data to the preferred source duration from grid-search for each explosive events. Event 4 and 5 do not fit the trend as their moment tensor solutions are poorly constrained. Right plot shows the raw waveform for event 1, 3 and 11. The pulse duration is measured from the first zero crossing before onset to the third zero crossing at the end of the signal.

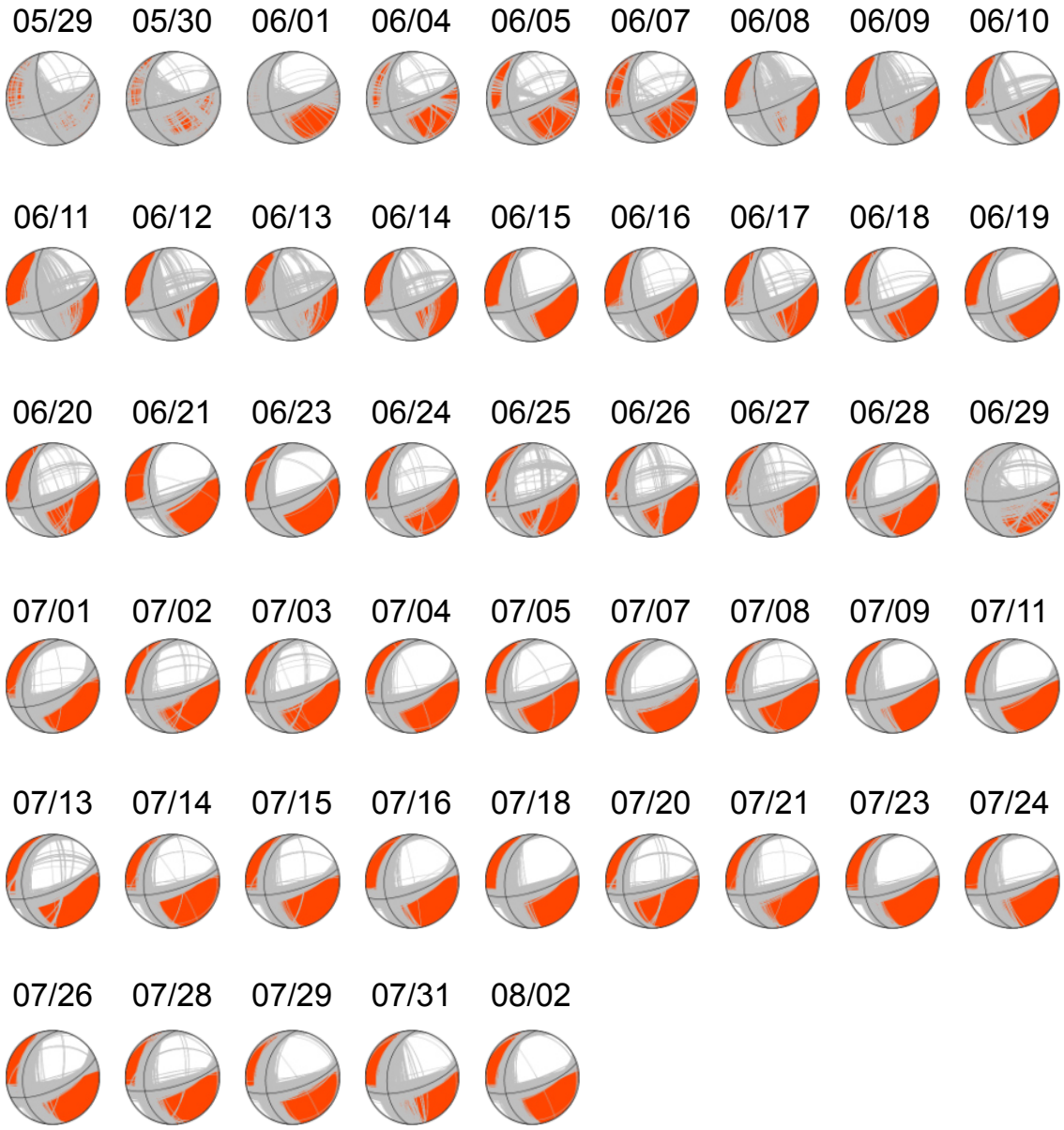

Figure S8:
Figure shows the bootstrapping results of the strike, rake, and dip for large collapse events between 05/29 and 08/02. The focal mechanism shows the double-couple contribution, the nodal planes from the bootstrapping (grey), and the preferred nodal planes (black) from the best-fitting full moment tensor solution. Despite the small number of stations, the bootstrapping results show consistent strike, rake, and dip for most events, indicating good constraint on the focal mechanism.

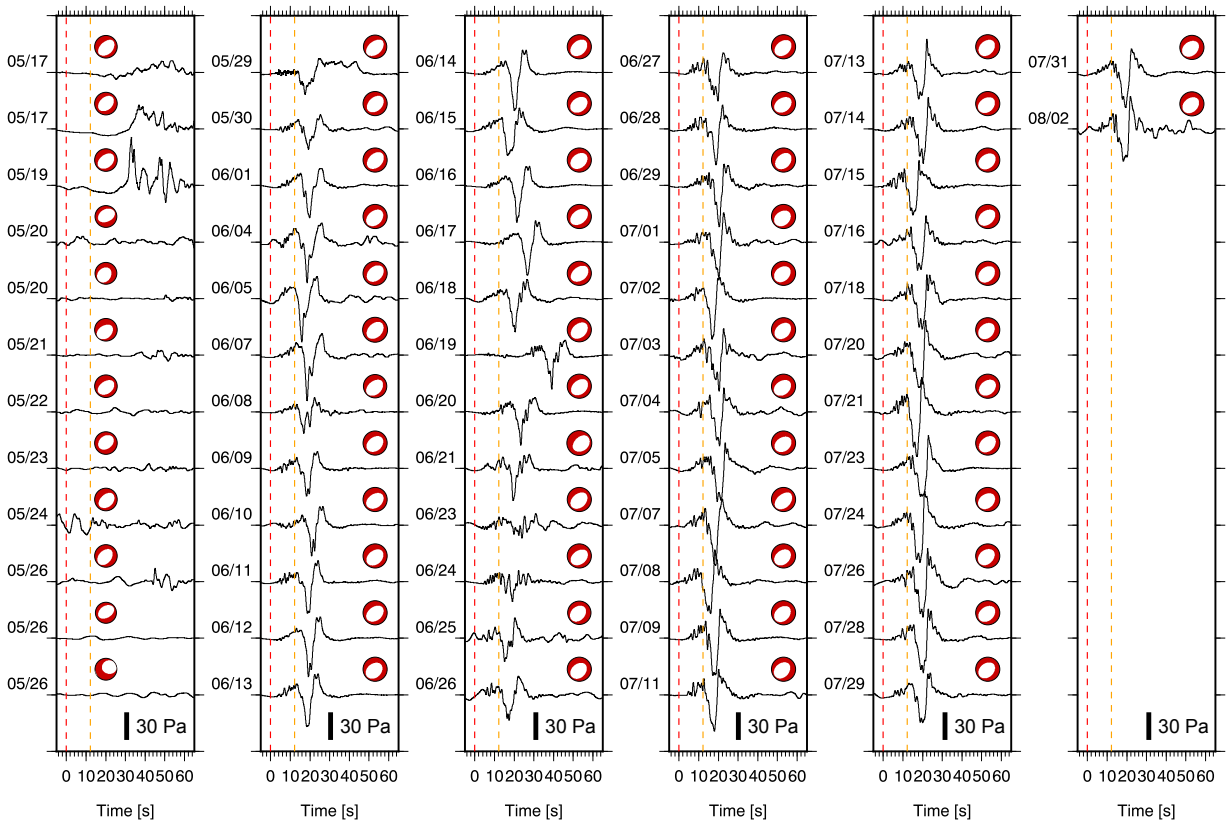

Figure S9:
Figure shows infrasound data recorded at AHUD and the Global Centroid Moment Tensor (GCMT) solutions for the 62 summit events. The infrasound data is deconvolved with the instrument response (last accessed July 2021) and filtered at 0.04 to 1 Hz. The data are plotted on the same amplitude scale. The red dashed line is a marker for origin time from catalog and the orange dashed line marks the expected arrival time of the infrasonic pulse traveling at acoustic speed (~340 m/s) from source to sensor. The GCMT solutions are similar for all events. The infrasound data, on the other hand, have two distinct patterns. Data from 05/17 to 05/26 vary greatly between each event and have no clear arrival at the expected time. Data from 05/29 onwards have a distinct high frequency signal followed by a strong downward pulse which travels at acoustic speed. Events 06/17 and 06/19 have complicated subevents and the catalog origin time is assigned to the first subevent. The delayed arrivals in comparison to other events, suggest the later subevent is responsible for the infrasound signal.

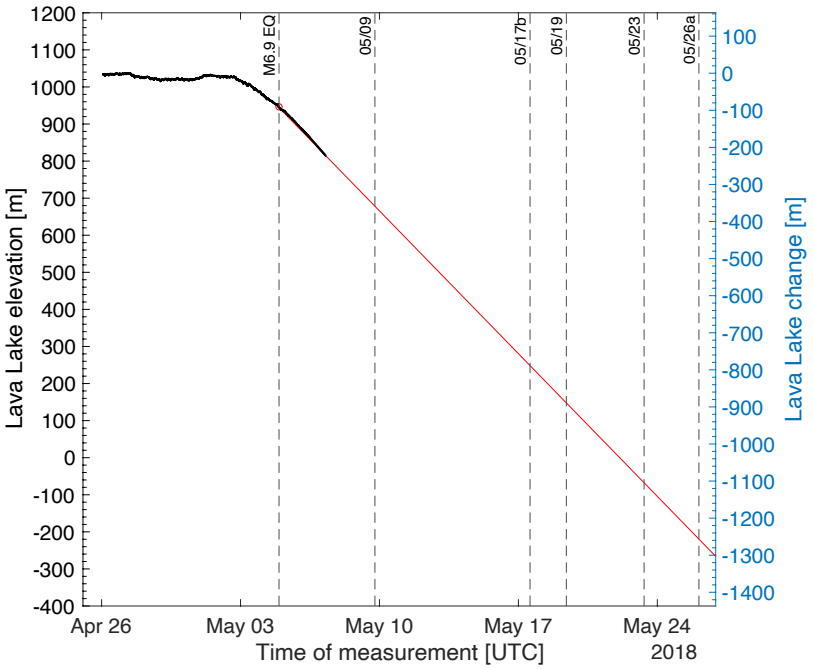

Figure S10:

Plot shows the lava lake elevation data measured from continuous laser rangefinder collected by USGS-HVO (black) and the estimated lava lake elevation change based on a constant draining rate of 2.2 meter per hour since the large M6.9 earthquake. By the end of the explosive events, the lava lake has dropped to a depth of ~1260 m. The data from the laser rangefinder can be obtained here: doi:10.5066/P9MJY24N

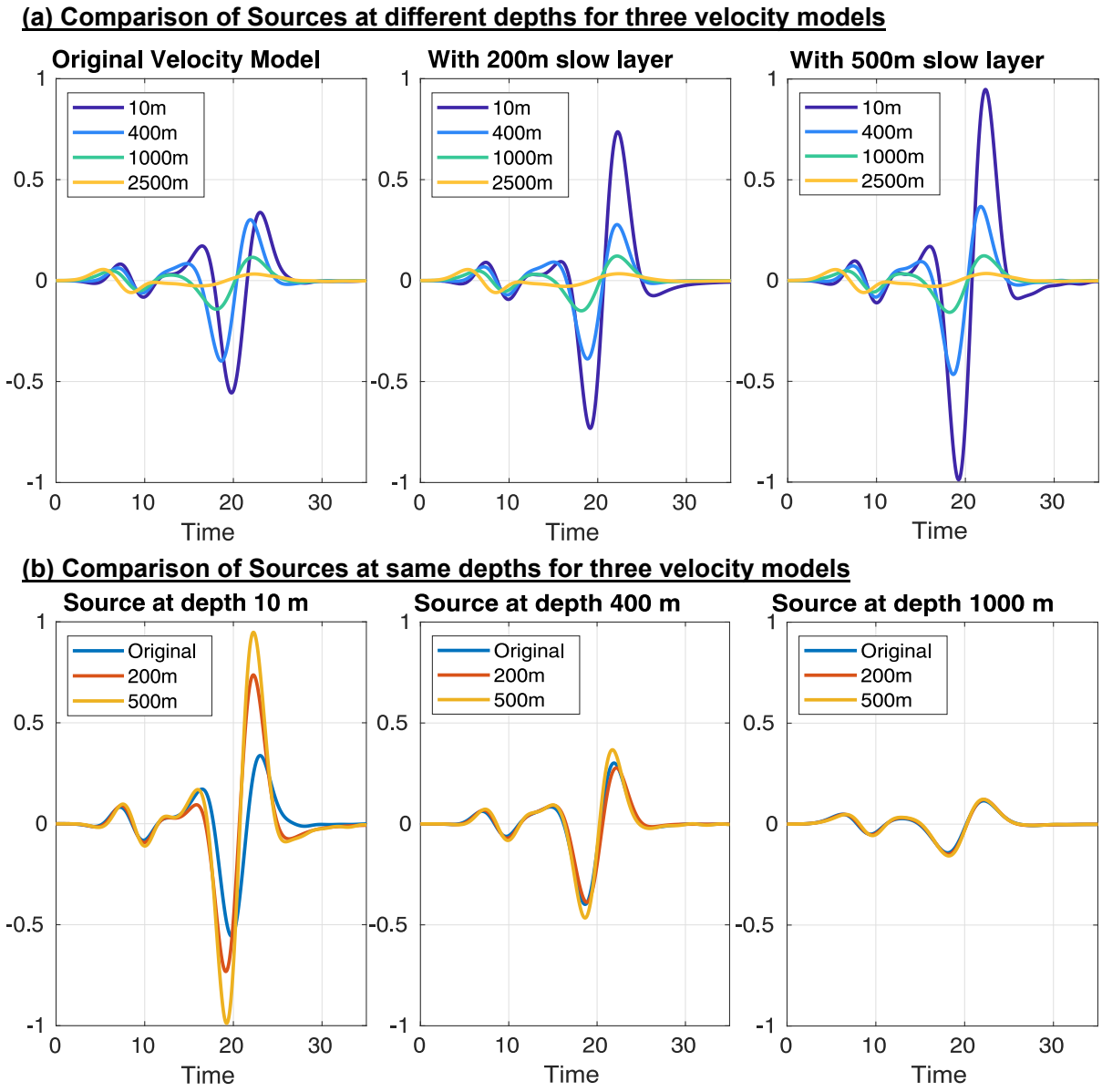

Figure S11:
(a) Plot shows the comparison of synthetics generated using the collapse solution (normal-faulting) at various depths with the 1-D velocity model used in the seismic inversions, and two modified velocity models in which the top 200 and 500 m are replaced with a slow layer. (b) Plot shows similar comparison but for synthetics at fixed source depth for the three velocity models. The synthetics show that the amplitude ratio between the acoustic and Rayleigh pulse is stronger for source at shallower depth. The amplitude ratio increases as well when there is a slow surface layer, particularly for sources at shallower depth. We can exclude sources at depth greater than 1 km, as the amplitude ratio is close to 1, which is not observed in data, and the ratio does not change greatly with velocity models.

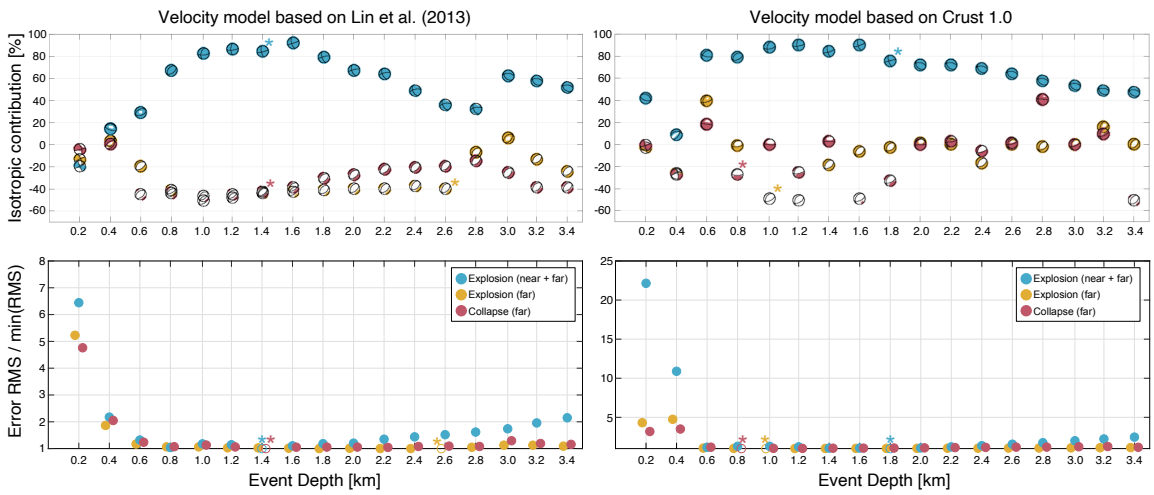

Figure S12:
Figure shows the effect of depth and availability of near field stations on the recovered full moment tensor solutions. We solve for the full moment tensor solutions using gCAP for three types of events: (blue) explosive event on May 17 (event 1) using all near field and regional stations; (yellow) same explosive event with regional stations only; and (pink) collapse event on July 20 with regional stations. Top row shows the isotropic contribution of the recovered moment tensors for event depths between 0.2 and 3.4 km for the two velocity models derived from Lin et al. (2013; this study) and Crust 1.0. Bottom row shows the distribution of error RMS with depth. The error RMS is normalized with the minimum RMS within each event category. The points have a slight offset for visual clarity. The best solutions have a normalized error RMS of 1 and are marked with color-coded asterisks. We found that the best moment tensor solutions without near-field stations consistently prefer deeper depths and have a negative isotropic contribution. Full moment tensor solutions for shallow depths are unstable due to the weak excitation of isotropic and dip-slip components.

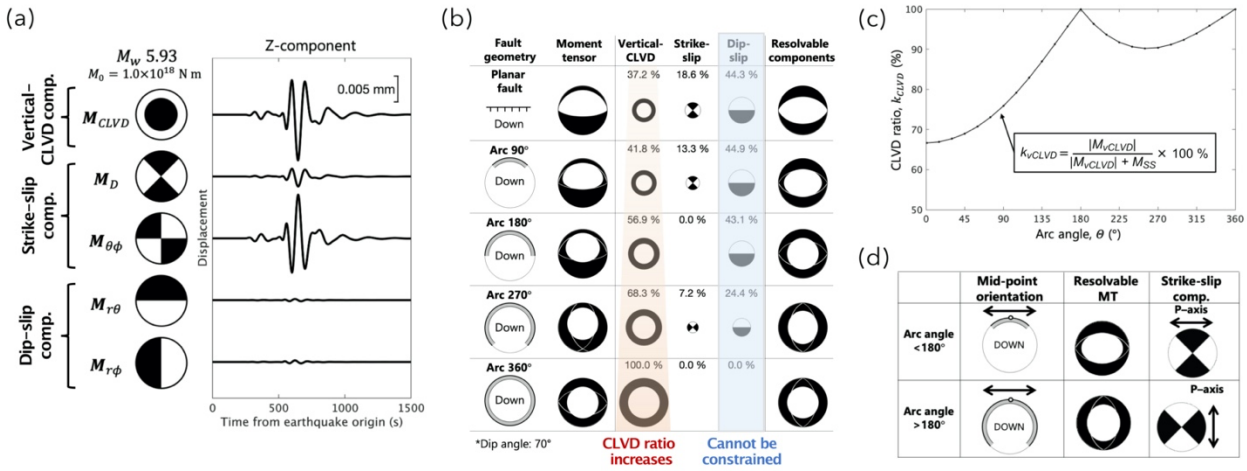

Figure S13:

(a) Figure illustrates that for a shallow earthquake, the vertical-CLVD and strike-slip components excite long period surface waves observable at teleseismic distances but not the dip-slip components ($M_{r\theta}$ and $M_{r\emptyset}$).

(b) Figure shows the theoretical moment tensor solution, their respective vertical-CLVD, strike-slip and dip-slip contributions, and resolvable moment tensor from teleseismic surface waves for planar fault slip, partial ring-fault slips and complete ring-fault slip. The CLVD ratio k_{CLVD} is sensitive to the arc angle of the ring fault that has slipped. k_{CLVD} is minimum (66.7%) for a linear fault. As the arc angle increases, M_{vCLVD} increases while M_{SS} decreases, resulting in an increase in k_{CLVD}. k_{CLVD} is maximum (100%) when the arc angle is 180° or 360° because M_{SS} is zero. The dip-slip components are not resolved by teleseismic surface waves.

(c) Graph shows the relationship between k_{CLVD} and the arc angle of the ring-fault slip, estimated from synthetic test. k_{CLVD} < ~80 % corresponds to small arc angle (< 180°).

(d) Figure shows two examples of caldera block dropping inward with partial ring-fault slip where the arc angles are < 180° and > 180°. The resolvable moment tensors look similar but their respective strike-slip component shows different orientation for the P-axis. For arc angle less than 180°, the P-axis is parallel to the tangent at the mid-point of the fault; for arc angle more than 180°, the P-axis is perpendicular to the tangent at the mid-point.

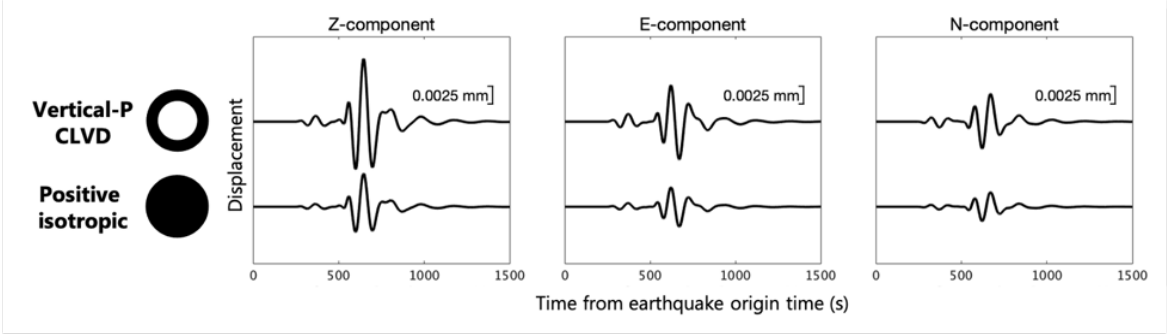

Figure S14:
Figure shows the similarity of teleseismic surface wave displacements for all three components produced by vertical-P CLVD and positive isotropic mechanisms, indicating a strong trade-off in resolving the vertical-P CLVD and isotropic contributions.

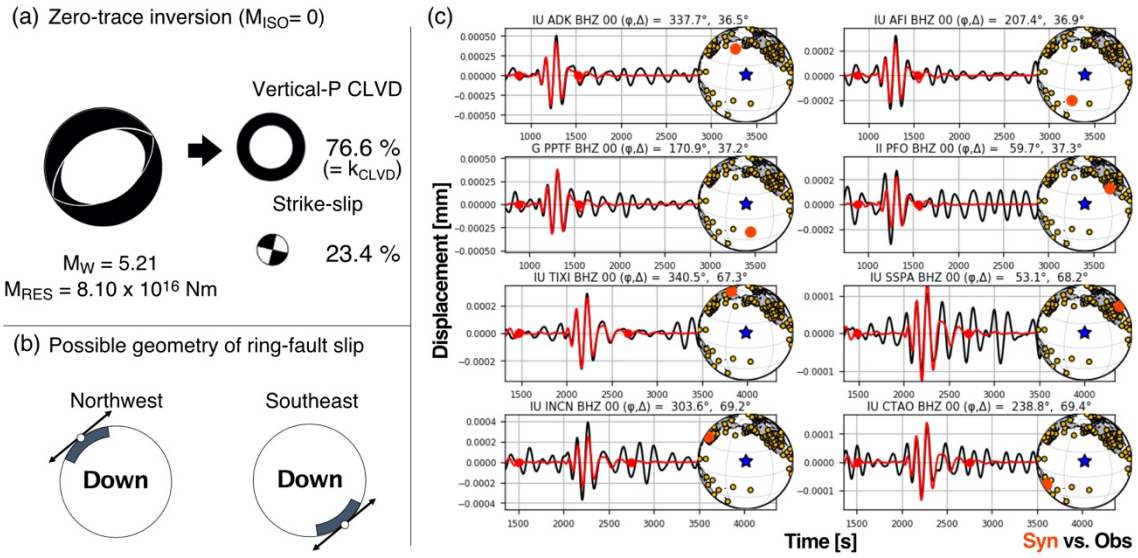

Figure S15.
Figure shows the inversion results for collapse event 17 using teleseismic waves filtered at 100 – 200 seconds: **(a)** inversion assumes zero trace ($M_{ISO} = 0$), yielding a ring-fault slip of M_{RES} = 8.10 x 10^{16} Nm (M_W = 5.21) with 76.6% vertical-P CLVD and 23.4% strike-slip; **(b)** Based on the inverted P-axis direction and the CLVD ratio (k_{CLVD}), the ring-fault slips partially along either the northwest or southeast corner of the caldera. **(c)** Plots show comparison of teleseismic waveform between data recorded at representative global stations and synthetics.

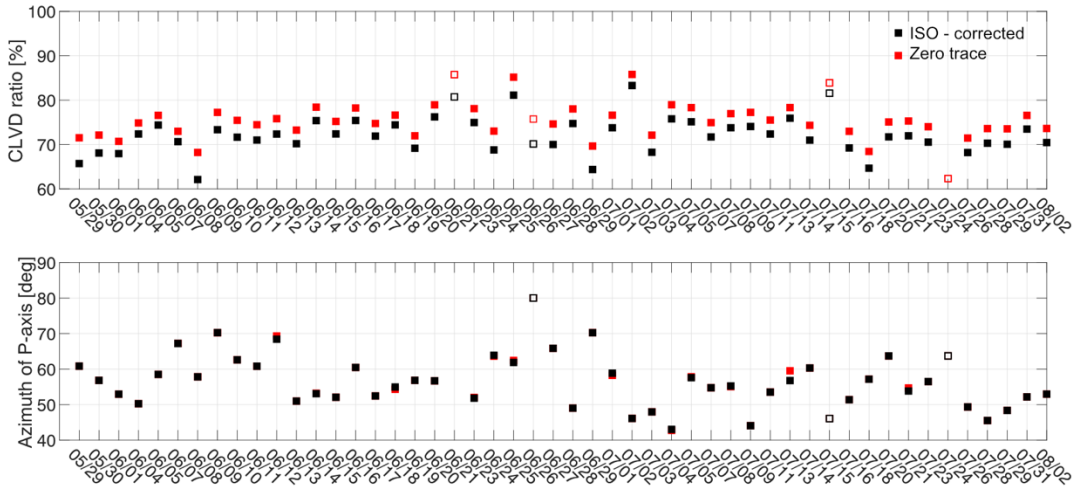

Figure S16:
Figure shows the CLVD ratio k_{CLVD} (top) and the azimuth of the P-axis from the strike-slip component (bottom) of the inversion results for the later 50 collapse events between 05/29 and 08/02. Results from the preferred inversion with isotropic correction (black) and inversion with zero trace constraint (red) are fairly similar. k_{CLVD} is between 65 and 80%, indicating partial collapse on ring fault with arc angle < 90°. The average azimuth of the P-axis is 60 degree away from the north, indicating the slip occurs along either the northwest or southeast corner of the ring fault. Inversion results performed with less than 20 seismic records are unreliable and marked by unfilled squares.

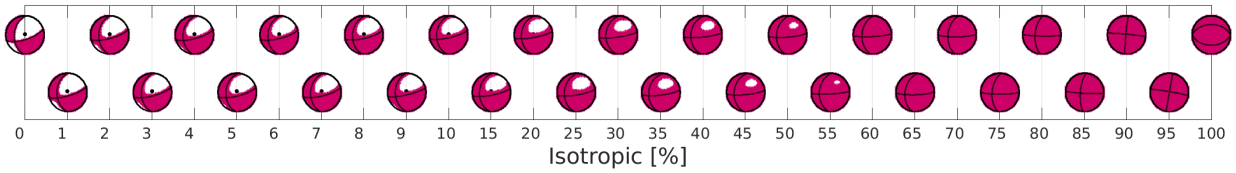

Figure S17:
Figure shows the fit of antipodal PKIKP (from Butler,2019; marked with a black dot) with focal mechanisms generated for a range of isotropic contribution. The CLVD contribution is fixed at zero. The only solutions that match with the dilatational polarity are solutions with very little isotropic contribution (< 5%).

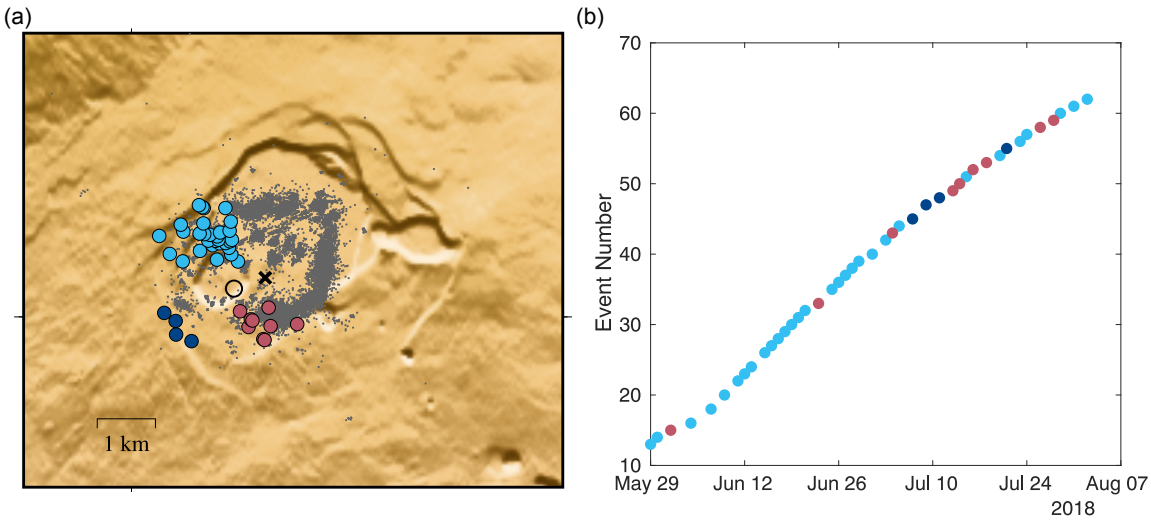

Figure S18:
(a) Map shows the location of the microseismicity cluster (grey dots) and large collapse events (colored circles) between 2018 May 29 and Aug 02 from Shelly and Thelen (2019). The circles are color-coded based on location. **(b)** Graph showing the event numbers and their respective location.

Data Set S1:

The csv file contains the moment tensor solutions for the early 12 explosive events and the 50 collapse events. The moments are given in N•m. Event 4 and 5 (marked with asterisk) have unreliable moment tensor solutions due to unusually long source duration.

Data Set S2: Moment tensor solutions for collapse events using global stations

The zipped file contains a Readme file and a catalog containing the teleseismic moment tensor solution with zero trace constraint for the 50 late collapse events (event 13 to 62). Both total and resolvable seismic scalar moments are provided for completeness but only the resolvable seismic scalar moment is reliable.